

## A Q2Q1 finite element/level-set method for simulating two-phase flows with surface tension

Myung H. Cho<sup>1</sup>, Hyoun G. Choi<sup>2,\*</sup>,<sup>†</sup>, Sang H. Choi<sup>3</sup> and Jung Y. Yoo<sup>1,3</sup>

<sup>1</sup>*Institute of Advanced Machinery and Design, Seoul National University, 599 Gwanak-ro, Gwanak-gu, Seoul 151-744, Korea*

<sup>2</sup>*Department of Mechanical Engineering, Seoul National University of Science and Technology, 172 Gongreung-2-dong, Nowon-gu, Seoul 139-743, Korea*

<sup>3</sup>*School of Mechanical and Aerospace Engineering, College of Engineering, Seoul National University, 599 Gwanak-ro, Gwanak-gu, Seoul 151-744, Korea*

### SUMMARY

A Q2Q1 (quadratic velocity/linear pressure) finite element/level-set method was proposed for simulating incompressible two-phase flows with surface tension. The Navier–Stokes equations were solved using the Q2Q1 integrated FEM, and the level-set variable was linearly interpolated using a ‘pseudo’ Q2Q1 finite element when calculating the density and viscosity of a fluid to avoid an unbounded density/viscosity. The advection of the level-set function was calculated through the Taylor–Galerkin method, and the direct approach method is employed for reinitialization. The proposed method was tested by solving several benchmark problems including rising bubbles exhibiting a large density difference and the surface tension effect. The numerical results of the rising bubbles were compared with the existing results to validate the benchmark quantities such as the centroid, circularity, and rising velocity. Furthermore, we focused our attention mainly on mass conservation and time-step. We observed that the present method represented a convergence rate between 1.0 and 1.5 orders in terms of mass conservation and provided more stable solutions even when using a larger time-step than the critical time-step that was imposed because of the explicit treatment of surface tension. Copyright © 2012 John Wiley & Sons, Ltd.

Received 21 December 2010; Revised 15 July 2011; Accepted 11 September 2011

KEY WORDS: finite element method; level set method; direct approach method; surface tension; rising bubble

### 1. INTRODUCTION

Problems of two-phase flows involving the interactions between a gas phase and a liquid phase have been encountered in a wide range of engineering applications such as ink-jet printing, atomization, blending, flow coating, internal combustion engine fuel spraying, container filling, etc. Various methods exist for the direct numerical simulation of two-phase flows. Major issues in such methods entail interface positioning and the treatment of effects induced by surface tension.

In principle, the positioning of interfaces in two-phase flows can be classified into front tracking methods and front capturing methods. Among the front capturing methods, the level set (LS) method [1,2] and the volume of fluid (VOF) method [3] have drawn the most attention. The LS method has an advantage over the VOF method in that the interface involving jump conditions is managed by a continuous and differentiable LS function, and that the extension of a two-dimensional (2D) code to a three-dimensional (3D) one is quite straightforward. However, the LS method has a disadvantage in that it is not readily mass-conservative and has to solve a reinitialization equation to maintain

\*Correspondence to: Hyoun G. Choi, Department of Mechanical Engineering, Seoul National University of Science and Technology, 172 Gongreung-2-dong, Nowon-gu, Seoul 139-743, Korea.

<sup>†</sup>E-mail: hgchoi@snut.ac.kr

the LS function as a signed distance function. This is because the values of the LS function do not remain as those of the distance functions right after an advection of the LS function is carried out [1]. Thus, the above-mentioned additional process of the LS method has to be carried out at each time step after advection. In fact, reinitialization has become an important issue in the LS method in the light of mass conservation [1]; thus, various methods [4–8] have been proposed for this process.

Modeling the surface tension effect is another major issue with regard to simulating two-phase flows, particularly in conjunction with the increasing interest in the fields of microfluidics and bubble dynamics. In 1992, Brackbill *et al.* [9] introduced the continuum surface force (CSF) model, which takes the surface tension term into consideration. This term has been widely used in the interface capturing method. However, this scheme possesses two major challenges: a significant time step limitation of, and spurious currents created by an imbalance between the surface tension and pressure gradient. Extensive research has been allotted to reducing these spurious currents. Hysing [10] and Hysing *et al.* [11] introduced a semi-implicit CSF model to overcome the time-step limitation and the spurious current problem, by exhibiting that the new model coupled with FEM provided more stable results in comparison to the original CSF model. Raessi *et al.* [12] implemented Hysing's semi-implicit CSF model with a finite volume method by showing that the method significantly alleviated the numerical capillary time-step limitation without destabilizing the solution. Sussman *et al.* [13] and Ye *et al.* [14] employed a sharp interface method. Sussman *et al.* [13] maintained the jump condition of pressure without any artificial smoothing and provided improved accuracy. However, the method caused numerical instability with regard to problems associated with high density ratios. On the other hand, Tong and Wang [15, 16] introduced the pressure boundary method (PBM) in which the surface tension effect was treated as a Dirichlet boundary condition. They showed that spurious currents were drastically suppressed and the sharp pressure boundary conditions were preserved. Hua and Lou [17] simulated the rising of a bubble in quiescent viscous liquid using an improved front-tracking method. They applied a new front-tracking method to investigate bubble rising and deforming behaviors in various flow regimes by expressing the bubble shape and velocity as a function of the parameters such as the Reynolds number, Bond number, density ratio, and viscosity ratio. Marchandise *et al.* [18] presented a quadrature-free DG method based on the LS method and successfully applied it to the problem in which gas bubbles rise in a viscous liquid. They also showed that a least-square computation of the curvature filters out the high frequencies and is more robust in comparison with the direct derivation of the LS function. Kang *et al.* [19] extended a ghost fluid method (GFM) proposed by Fedkiw *et al.* [20] to 3D multiphase incompressible flow considering the effects of viscosity and surface tension.

In this work, the Taylor–Galerkin/direct reinitialization approach of the LS method proposed by Cho *et al.* [21], which was combined with a four-step fractional Q1Q1 (linear velocity/linear pressure) FEM, is extended to an integrated Q2Q1 (quadratic velocity/linear pressure) FEM for simulating two-phase flows with surface tension. The LS variable is interpolated linearly or quadratically and the surface tension effect is treated by the CSF model [9]. Several benchmark problems involving Rayleigh–Taylor instability, spurious currents, bubble rising in a partially-filled container, and bubble rising in a fully-filled container are solved for validation. The present numerical results are compared with the existing results and examined in terms of mass conservation and time step.

## 2. NUMERICAL METHOD

In the present finite element simulation, the incompressible Navier–Stokes equations were discretized using a Q2Q1 element (see Figure 1(a)) for spatial discretization and Crank–Nicolson method for temporal discretization. The Taylor–Galerkin scheme was employed for the advection equation of the LS function. Moreover, the direct approach method [21] was adopted to reinitialize the LS function instead of solving the hyperbolic type equation. The effect of surface tension acting at the interface was considered using a CSF model [9]. In the following three subsections, the numerical methods used in this study are explained in detail.

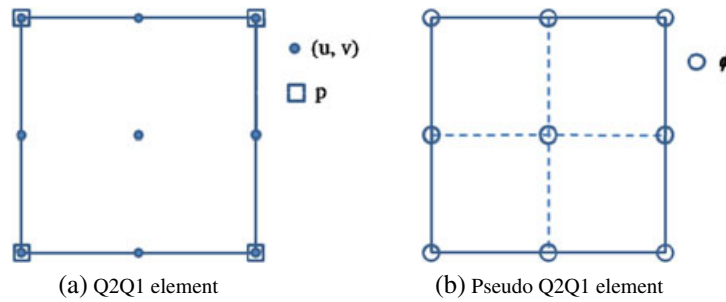


Figure 1. Q2Q1 element used.

### 2.1. Governing equations

The governing equations for simulating a two-phase flow are the incompressible Navier–Stokes equations coupled with the advection equation of the LS variable, which can be written as follows:

$$\nabla \cdot \mathbf{u} = 0, \quad (1a)$$

$$\rho(\phi) \frac{D\mathbf{u}}{Dt} = -\nabla p + \nabla \cdot [\mu(\phi) (\nabla \mathbf{u} + \nabla \mathbf{u}^T)] + \sigma \kappa(\phi) \delta(\phi) \mathbf{n} + \rho(\phi) \mathbf{g}, \quad (1b)$$

$$\frac{\partial \phi}{\partial t} + \mathbf{u} \cdot \nabla \phi = 0, \quad (1c)$$

where  $\phi$ ,  $\rho(\phi)$ ,  $\mu(\phi)$ ,  $\kappa(\phi)$ ,  $\delta(\phi)$  denote the LS function, the density, the dynamic viscosity of the fluid, the curvature of an interface, and the Dirac-delta function, respectively;  $\sigma$ ,  $\mathbf{n}$ ,  $\mathbf{g}$  represent the coefficient of surface tension, unit normal to the interface, and gravity, respectively. The effect of surface tension is treated in an explicit way using the CSF method [9], where the continuous pressure profile and Dirac-delta function are used. In the case of the LS method, to prevent the fluid properties from sudden changes, the interface was assumed to be of finite thickness (smooth zone), which is defined by the level set function  $\phi$  such that  $|\phi| \leq \varepsilon$ , where  $\varepsilon$  is set to  $2h$  with  $h$  being an element characteristic length near the interface. Then, the smoothed Heaviside function  $H(\phi)$  can be defined as follows:

$$H(\phi) = \begin{cases} 0 & \text{if } \phi < -\varepsilon \\ \frac{1}{2} \left[ 1 + \frac{\phi}{\varepsilon} + \frac{1}{\pi} \sin\left(\frac{\pi\phi}{\varepsilon}\right) \right] & \text{if } |\phi| \leq \varepsilon \\ 1 & \text{if } \phi > \varepsilon \end{cases}, \quad (2)$$

through which the density and viscosity are computed as follows:

$$\begin{aligned} \rho(\phi) &= \rho_g + (\rho_l - \rho_g) H(\phi), \\ \mu(\phi) &= \mu_g + (\mu_l - \mu_g) H(\phi), \end{aligned} \quad (3)$$

where the subscripts g and l denote gas and liquid, respectively.

### 2.2. Q2Q1 finite element formulations for the incompressible Navier–Stokes equations

In the previous study [21] on the direct reinitialization method for the LS function, the surface tension effect could not be included in the formulation because the splitting FEM was not appropriate for the simulation of surface-tension dominant flows in which strong pressure jumps across the interface exist. Some of the previous studies on splitting methods [22, 23], for which a separate elliptic-type pressure equation obtained from the continuity constraint is solved, revealed that the intermediate velocity field of a splitting method may poorly approximate the velocity field at time-step  $(n+1)$  when the pressure field varies greatly in space and time as in the case of surface-tension dominant flows and the continuity constraint is not strictly satisfied. Therefore, a monolithic Q2Q1

FEM was adopted for the present simulation of surface-tension dominant flows using the direct reinitialization method. Discontinuous pressure approximation based on particle FEM [24, 25] or a boundary capturing method [19] based on GFM can accurately simulate the pressure jump across the interface because the pressure is discontinuous at the interface because of surface tension and because of the difference between viscosities. Nonetheless, the present study uses a continuous pressure approximation (linear pressure interpolation) and the effect of surface tension was treated by CSF method [9] because the conventional Q2Q1 FEM, which satisfies the Babuška–Brezzi condition [26], was adopted for solving the incompressible Navier–Stokes equations. Therefore, in this study, the pressure jump across the interface because of surface tension or difference between viscosities can be represented only by using a fine mesh near the interface. The Galerkin formulation of Equations (1a) and (1b) is obtained by multiplying Equations (1a) and (1b) by weighting functions  $q$  and  $\mathbf{W}$ , respectively, and then integrating by parts the stress terms of Equation (1b) by means of the divergence theorem. The Galerkin formulation of Equations (1a) and (1b) is then written as follows:

Find  $u_i \in H^1(\Omega)$ ,  $p \in L^2(\Omega)$  such that

$$\int_{\Omega} \left\{ \mathbf{W} \cdot \rho(\phi) \left[ \frac{D(\mathbf{u} - \mathbf{u}_m)}{Dt} - \mathbf{g} \right] - \mathbf{W} \cdot \sigma \kappa(\phi) \delta(\phi) \mathbf{n} + \nabla \mathbf{W} : [-p \tilde{\mathbf{I}} + \mu(\phi) (\nabla \mathbf{u} + \nabla \mathbf{u}^T)] \right\} d\Omega - \int_{\Gamma_2} \mathbf{W} \cdot \{ [-p \tilde{\mathbf{I}} + \mu(\phi) (\nabla \mathbf{u} + \nabla \mathbf{u}^T)] \cdot \mathbf{n} \} d\Gamma_2 + \int_{\Omega} q (\nabla \cdot \mathbf{u}) d\Omega = 0, \quad (4)$$

for all  $W_i \in V$  and  $q \in P$ , where  $V = \{W_i | W_i \in H^1(\Omega), W_i = 0 \text{ on } \Gamma_1\}$ ,  $P = \{q | q \in L^2(\Omega)\}$ ,  $\tilde{\mathbf{I}}$  is the second-order identity tensor,  $\Gamma$  is the boundary of  $\Omega$ ,  $\mathbf{n}$  is the outward unit normal vector to  $\Gamma$  and  $\mathbf{u}_m$  is the mesh velocity.  $H^1$  denotes a space of functions defined on the spatial domain  $\Omega$  of which the first derivative is square-integrable and  $L^2$  denotes a space of square-integrable functions. Velocity variable of the Navier–Stokes equations is interpolated by using vector functions belonging to the space  $H^1$  and pressure variable by functions belonging to the space  $L^2$ .

After performing numerical integration for Equation (4) by nine-point Gaussian quadrature rule, the following saddle-point type global matrix is obtained:

$$\begin{pmatrix} A & B \\ B^T & 0 \end{pmatrix} \begin{pmatrix} \mathbf{u} \\ p \end{pmatrix} = \begin{pmatrix} \mathbf{f} \\ 0 \end{pmatrix}. \quad (5)$$

The saddle-point type matrix given in Equation (5) was solved by Bi-CGSTAB (bi-conjugate gradient stabilized) [27] with an adapted ILU (AILU) preconditioner [28]. The successive-substitution method was used to treat the nonlinearity of the momentum equations.

In Equation (4),  $\phi$  is linearly interpolated using a ‘pseudo’ Q2Q1 element shown in Figure 1(b) when evaluating the density and viscosity of the fluid in the momentum equation to avoid an unbounded value. Figure 2 illustrates that a negative fluid viscosity/density may occur from

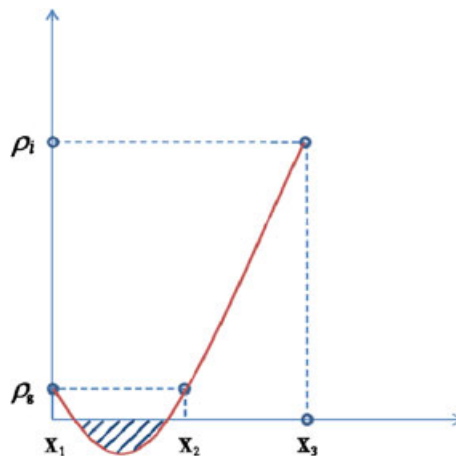


Figure 2. Negative fluid viscosity/density possibly resulting from quadratic-interpolation.

quadratic interpolation. Therefore, the density and viscosity of the fluid at Gauss-integration points are directly calculated for the Q2Q1 elements within the smoothing zone;  $\phi$ 's at Gauss-integration points are obtained using the direct approach method explained in Section 2.4 so that the density and viscosity of the fluid at those points are calculated using Equation (3). On the other hand,  $\phi$  is interpolated quadratically to utilize high-order interpolation for calculating the curvature  $\kappa(\phi)$ , which is obtained using the following formula:

$$\kappa(\phi) = -\nabla \cdot \vec{n} = -\nabla \cdot \left( \frac{\nabla \cdot \phi}{|\nabla \cdot \phi|} \right) = -\frac{\phi_y^2 \phi_{xx} - \phi_x \phi_y \phi_{xy} + \phi_x^2 \phi_{yy}}{(\phi_x^2 + \phi_y^2)^{3/2}}, \quad (6)$$

where the first derivatives of  $\phi(\phi_x, \phi_y)$  are interpolated quadratically, whose nodal values are obtained using the least-squares method. Then, the second derivatives of  $\phi$  are derived from the first derivatives,  $\phi_x$  and  $\phi_y$ .

### 2.3. Advection equation of LS function

After solving the incompressible Navier–Stokes equations coupled with the LS variable, the advection equation of the LS function Equation (1c) was solved to update an interface in the two-phase flow. In the present study, the LS variable for the advection equation was interpolated linearly using the ‘pseudo’ Q2Q1 element, as explained in Section 2.2. The Taylor–Galerkin finite element formulation, which was used by Cho *et al.* [21], was adopted for stabilizing the advection equation of the hyperbolic type. The Taylor–Galerkin finite element formulation was derived by inserting a Taylor series expansion of  $\phi$  into the advection Equation (1c) [29, 30] so that the final form of the formulation is written as follows:

$$\begin{aligned} \int_{\Omega_e} \mathbf{W} (\phi^{n+1} - \phi^n) d\Omega = & -\Delta t \int_{\Omega_e} \mathbf{W} (\mathbf{u}^{n+1} \cdot \nabla) \phi^{n+1} d\Omega \\ & + \underbrace{\frac{\Delta t^2}{2} \int_{\Omega_e} \mathbf{W} (\mathbf{u}^{n+1/2} \cdot \nabla) \left[ (\mathbf{u}^{n+1/2} \cdot \nabla) \phi^{n+1} \right] d\Omega}_C. \end{aligned} \quad (7)$$

The second term  $C$  on the right-hand side of Equation (7) can be written as follows by applying the integration by parts and the divergence theorem of Gauss:

$$C = - \int_{\Omega_e} u_i^{n+1/2} \frac{\partial \mathbf{W}}{\partial x_i} u_j^{n+1/2} \frac{\partial \phi^{n+1}}{\partial x_j} d\Omega + \int_{\Gamma_e} \mathbf{W} n_i u_i^{n+1/2} u_j^{n+1/2} \frac{\partial \phi^{n+1}}{\partial x_j} d\Gamma, \quad (8)$$

where  $\Gamma_e$  denotes the surface of the computational domain  $\Omega_e$  and  $n_i$  is the unit outward normal to  $\Gamma_e$ . For the no-slip condition at the wall and the zero gradient conditions of  $\phi$  at the inlet and outlet, the surface integral may be omitted. A detailed procedure for the derivation of Equation (7) can be found in [21].

### 2.4. Direct reinitialization method of LS function

Because the LS function cannot always be the distance function after advection by the fluid velocity field, the reinitialization of the LS function is required. In this study, the direct approach method [21] was employed to reinitialize the LS function after advection. As in the advection equation, reinitialization was conducted by assuming that the LS variable was interpolated linearly on the ‘pseudo’ Q2Q1 element. As shown in Figure 3, the interface is approximated by  $\phi$  in each subelement, after advection is carried out. Among the node points ( $\mathbf{x}$ ),  $\mathbf{x}_1$ , and  $\mathbf{x}_2$  are respectively those in the liquid side and the gas side of subelement segments, which are intersected by the interface. Then, the position vector,  $\mathbf{x}_s$ , of the intersection of the subelement face and the interface is determined for each subelement by linear interpolation from the values of  $\phi$  at the ends of the corresponding subelement face

$$\mathbf{x}_s = \mathbf{x}_1 - \frac{\phi_1}{\phi_1 - \phi_2} (\mathbf{x}_1 - \mathbf{x}_2). \quad (9)$$

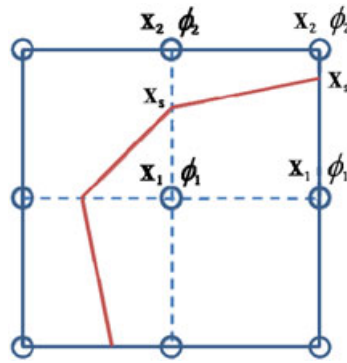


Figure 3. Subelement interfaces of a pseudo-Q2Q1 element.

The reinitialization process was performed for all nodes whose level set values were less than  $4h$  and the nodes adjacent to the interface, which was determined from Equation (9). The LS values of those nodes were updated by directly calculating the shortest distance to the interface. A detailed procedure for the direct reinitialization process can be found in [21].

### 3. RESULTS

#### 3.1. Rayleigh–Taylor instability

To validate the advection and the reinitialization schemes used in the present numerical method, we tested an air/helium Rayleigh–Taylor instability problem, which was solved by Bell and Marcus [31] and Puckett *et al.* [32] using the VOF method, and Popinet and Zaleski [33] using the front tracking method. To compare the present result with that of Puckett *et al.* [32], we chose the computational domain to be a  $0.01 \times 0.04$  m rectangle, as shown in Figure 4, by imposing a  $121 \times 481$  uniform grid. The densities and viscosities of the two fluids were  $1.225$ ,  $0.1694$  kg/m<sup>3</sup> and  $1.776 \times 10^{-5}$ ,  $1.941 \times 10^{-5}$  kg/(m·s), respectively. As shown in Figure 4, a heavy fluid lies above a light fluid and no-slip boundary condition is imposed on the vertical walls. The initial velocity field was zero and

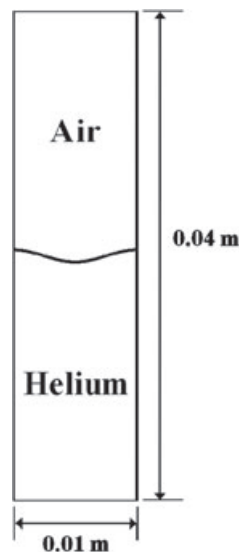


Figure 4. Illustration of the Rayleigh–Taylor instability problem.



the initial interface between the fluids was given as a sinusoidal perturbation of amplitude 0.5 mm as follows:

$$\phi = y + 0.0005 \cos\left(\frac{2\pi x}{0.01}\right). \quad (10)$$

The time-step used was  $5.0\text{E-}5$  s and the corresponding maximum CFL number was 0.307. Figure 5 shows the evolution of the interface at times, 0.05, 0.065, 0.09, and 0.12 s. Our results agree well with those of Puckett *et al.* [32].

### 3.2. Spurious currents

In this section, we consider a circular static bubble of radius  $R$  under zero gravity and viscosity to measure the dimensionless magnitude ( $Ca = U\mu/\sigma$ ) of the spurious currents. The pressure distribution inside and outside the bubble was determined by the Laplace–Young law as follows:

$$p_{\text{in}} = p_{\text{out}} + \sigma/R. \quad (11)$$

Ideally, both the velocity and pressure fields should be zero everywhere all the time. However, spurious velocities may be created by the imbalance between the pressure gradient and the surface tension across the interface, which are designated as spurious (parasitic) currents in previous literature [10, 18, 33, 34]. Thus, the computational domain was taken to be a  $4 \times 4$  m square and the bubble radius  $R = 1$  m, where the centers of the computational domain and the bubble coincided. We set the density and viscosity equal to 1 in the entire computational domain and imposed no-slip boundary condition on the vertical and horizontal walls. The gravity was neglected and the surface

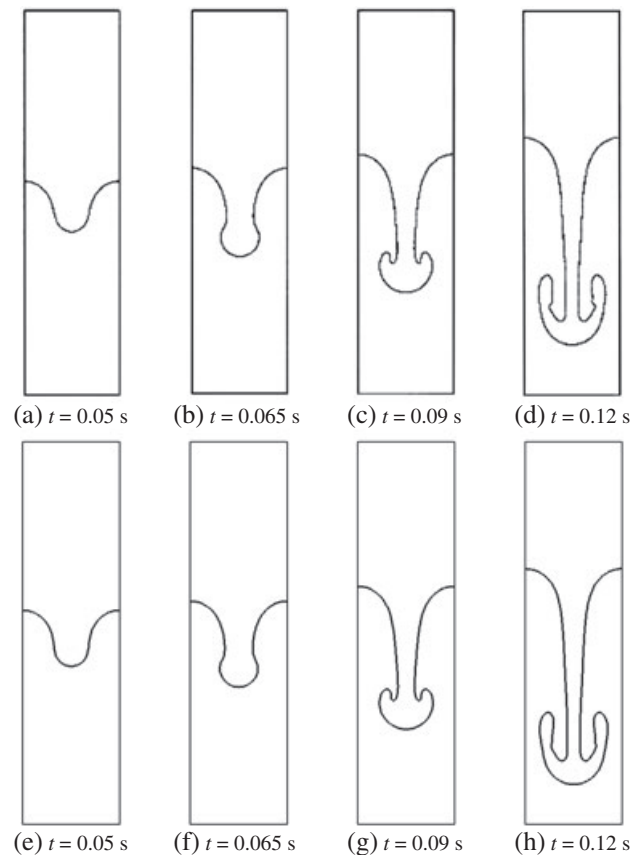
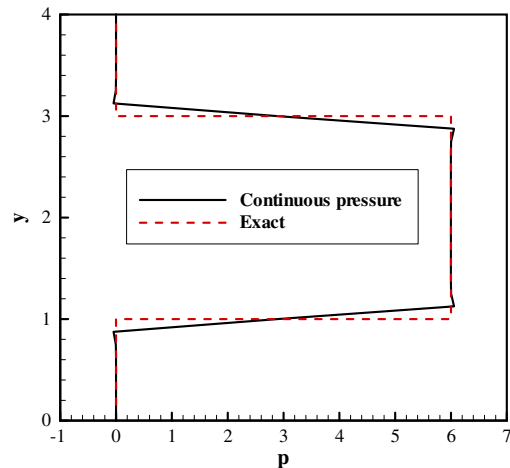


Figure 5. Evolution of the interface in the Rayleigh–Taylor instability at various times: (a)–(d) results of Puckett *et al.* [32] (permission for reproduction was granted by Academic Press); (e)–(h) present results.

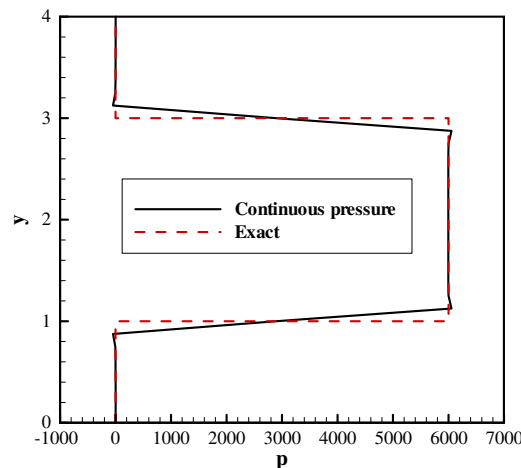
tension coefficient  $\sigma$  was varied to yield various Laplace numbers  $La(= 2R\sigma\rho/\mu^2)$ . The computation was performed until  $t = 250 \times d\mu/\sigma$  (s) at the moment when  $Ca$  was measured. Lafaurie *et al.* [34] conjectured that the magnitude of the spurious current was proportional to  $\sigma/\mu$ . Table I shows that  $Ca$  is nearly constant over a broad range of  $La$  when the grid size is  $h = L/32$  and that  $Ca$ 's of the present study are comparable to those of Marchandise *et al.* [18]. Figure 6 shows the pressure cuts at diametral plane  $x = 2.0$  for a circular bubble in static equilibrium, where the pressure differences between the inside and the outside of the bubble are  $\Delta p = \sigma/R = 6$  and  $6000$  N/m<sup>2</sup>, respectively, in the cases of  $La = 12$  and  $12,000$ . Table II shows the convergence rate of  $Ca$  with grid resolution in the case of  $La = 200$ . As shown in Table II and Figure 7, the present method exhibits nearly a first-order convergence, which was also coincident with the result of Marchandise *et al.* [18].

Table I. Independence of  $Ca$  from  $La$  (mesh size  $h = L/32$ ).

$La = d\sigma\rho/\mu^2$	12	120	1200	12,000
Present study	1.238E-4	1.236E-4	1.245E-4	1.140E-4
Marchandise <i>et al.</i> [18]	8.51E-5	8.62E-5	8.59E-5	8.31E-5



(a)  $La = 12$



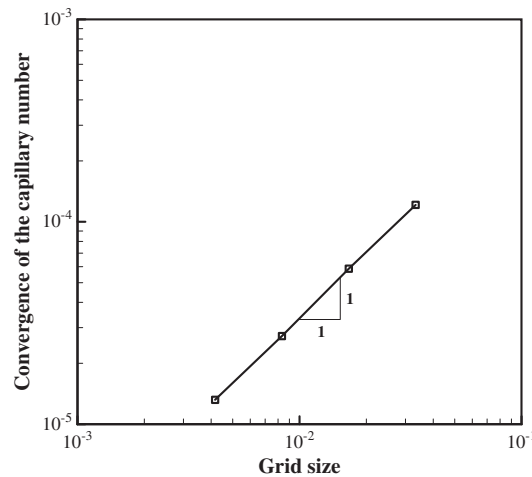
(b)  $La = 12000$

Figure 6. Pressure cuts at the diametral plane  $x = 2.0$  for a circular bubble in static equilibrium.



Table II. Convergence of  $Ca$  with spatial resolution ( $La = 200$ ).

$h$	$L/30$	$L/60$	$L/120$	$L/240$
Present study	1.212E-4	5.864E-5	2.726E-5	1.320E-5
Marchandise <i>et al.</i> [18]	1.29E-4	6.43E-5	3.18E-5	1.12E-5

Figure 7. Convergence rate of the capillary number versus grid size ( $La = 200$ ).

### 3.3. Bubble rising in a partially filled container

A two-dimensional bubble of fluid 2 rising in a container partially filled with fluid 1 was investigated, as shown in Figure 8. The computational domain was a  $0.12 \times 0.14$  m rectangle. The densities of fluid 1 and fluid 2 were  $1000 \text{ kg/m}^3$  and  $500 \text{ kg/m}^3$ , respectively, while the dynamic viscosities of fluid 1 and fluid 2 were  $0.12522 \text{ kg/m-s}$  and  $0.06261 \text{ kg/m-s}$ , respectively. The initial diameter of the bubble  $D_0$  was  $0.04$  m. The computational grid was composed of uniform grids, which had 67,721 nodes, and 16,800 rectangular elements. Two cases were considered: Case 1 without considering the surface tension effect and Case 2 considering the surface tension effect. The Reynolds number ( $Re$ ) and the Bond number ( $Bo$ ) are defined as follows:

$$Re = \frac{\rho_1 \sqrt{g} D_0^{1.5}}{\mu_1}, \quad Bo = \frac{\rho_1 g D_0^2}{\sigma}, \quad (12)$$

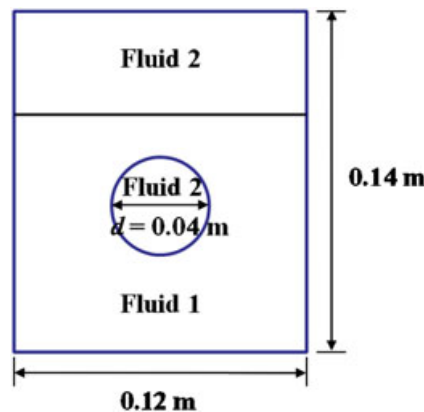


Figure 8. Schematic diagram of a 2D container partially filled with fluid 1, inside which a bubble of fluid 2 is rising.

where  $g$ ,  $\rho_1$ ,  $\mu_1$ , and  $\sigma$  ( $= 1.568$  N/m) are the gravity, density and viscosity of fluid 1, and surface tension coefficient, respectively. For both Cases,  $Re = 200$  is taken, while  $Bo = 10$  for Case 2. Computations were conducted until  $t = 0.24$  s with various time-steps. Figures 9 and 10 show the evolutions of bubble fluid 2 shape and velocity vector for Cases 1 and 2, respectively, with a time

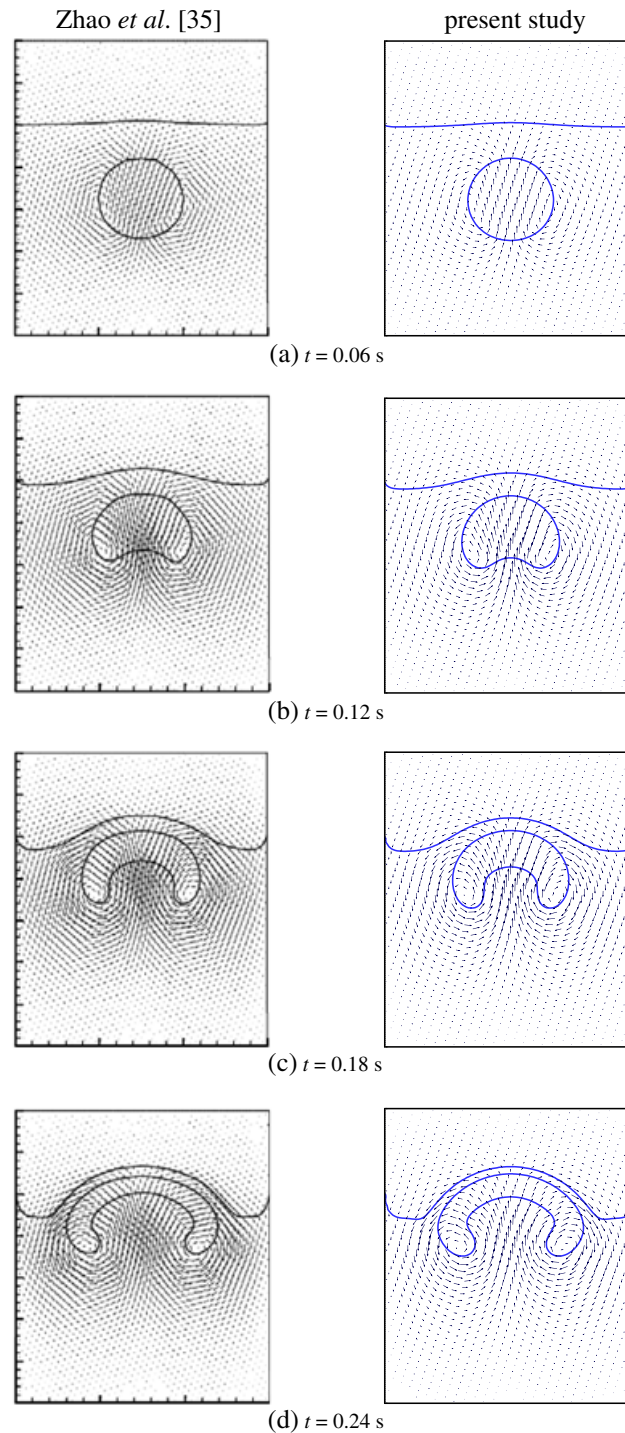


Figure 9. Time evolution of fluid 2 rising in a container partially filled with fluid 1, where the surface tension is not considered ( $Re = 200$ ) (permission for reproduction was granted by Elsevier Science).

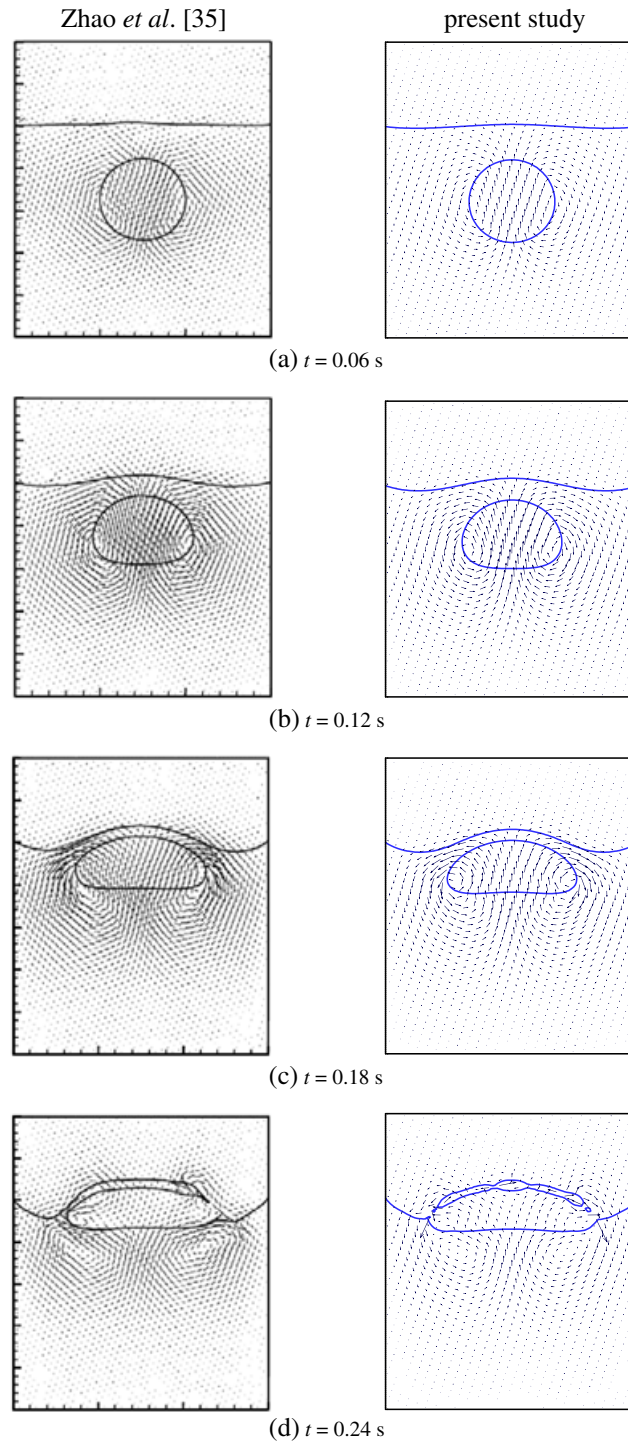


Figure 10. Time evolution of fluid 2 rising in a container partially filled with fluid 1, where the surface tension is considered ( $Re = 200$ ,  $Bo = 10$ ) (permission for reproduction was granted by Elsevier Science).

step of  $1.0E-4$ . Fluid 2 was accelerated because of the buoyancy force induced by the difference of densities between the two fluids. In Case 1, fluid 2 was deformed, taking a kidney shape. Fluid 2 continued to be deformed as it approached the interface between fluid 1 and fluid 2, resulting in the elongation of fluid 2 to both sides. At  $t = 0.18$  s, fluid 2 almost hits the interface. Next, in Case

2, fluid 2 behaved similarly to Case 1 until time  $t = 0.06$  s. However, after this, a kidney-shaped fluid 2 was no longer observed because of surface tension. Moreover, two vortices were observed below both sides of fluid 2. Our results compared well with those of Zhao *et al.* [35] for both Cases. The mass error (0.18 %) without surface tension effect was a little bit larger than that (0.044 %) with surface tension effect for a maximum time step of  $6.0\text{E-}4$  s. The mass error of a rising bubble is caused because of the force unbalance at the interface in the case of the surfacetension dominant flow and also because of the error introduced by the reinitialization/advection algorithm of the level-set method. Therefore, it is conjectured that the mass error without surface tension was larger than that with surface tension in the present simulation probably because the error introduced by the reinitialization/advection algorithm of the present level-set method in Case 1 dominates the error because of the force unbalance at the interface in Case 2. In any event, mass was conserved well within 0.2% during the entire simulation for a time-step of  $6.0\text{E-}4$  s. Table III shows the mass errors for Case 2 when various time steps were adopted. According to the study by Brackbill *et al.* [9], the time-step restriction because of the explicit treatment of surface tension is given as follows:

$$\Delta t_{\text{num}}^{\text{ca}} = \sqrt{\frac{\rho}{\sigma}} h^{3/2}. \quad (13)$$

Thus, the time-step restriction estimated by Equation (13) for Case 2 was  $2.0\text{E-}4$  s. Table III shows that the present simulations were stable for  $\Delta t \leq 3\Delta t_{\text{num}}^{\text{ca}}$  and mass errors were less than 0.5% for all the simulations. Figure 11 also shows that the contours of  $\phi = 0$  obtained using various time steps all collapse into a single contour at  $t = 1.8$  s in Case 2. It is noteworthy that the

Table III. Mass error for the bubble rising in a partially-filled container (Case 2:  $Re = 200$ ,  $Bo = 10$ ,  $\Delta t_{\text{num}}^{\text{ca}} = 2.0\text{E-}4$  s).

Time step size	$8 \times \text{E-}4$ s	$6 \times \text{E-}4$ s	$4 \times \text{E-}4$ s	$2 \times \text{E-}4$ s	$1 \times \text{E-}4$ s
Mass error (%)	Unstable	0.044	-0.193	-0.341	-0.416

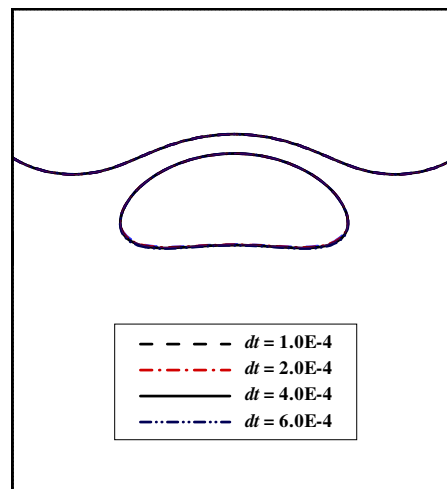


Figure 11. Shapes of the bubble of fluid 2 at  $t = 0.18$  s for various time steps.

Table IV. Physical parameters and dimensionless numbers.

Test case	$Re$	$Bo$	$\rho(\text{kg/m}^3)$		$\mu(\text{kg/m} \cdot \text{s})$		$g$ (kg/m <sup>2</sup> )	$\sigma$ (N/m)
			Fluid 1	Fluid 2	Fluid 1	Fluid 2		
A	35	10	1000	100	10	1	0.98	24.5
B	35	125	1000	1	10	0.1	0.98	1.96

present method gives a stable solution using a time step, which was three times larger than the time-step restriction in spite of the explicit treatment of the surface tension. As stated in Section 2.2, the present method solves the Navier–Stokes equations in a fully coupled manner, so that both the velocity and pressure variables are obtained simultaneously unlike other splitting (projection) methods [1, 10–13, 19, 24, 25]. Therefore, it is conjectured that the enhanced stability of the present monolithic approach is attributed to a fully-implicit treatment of pressure in the momentum equation, which balances the surface tension force.

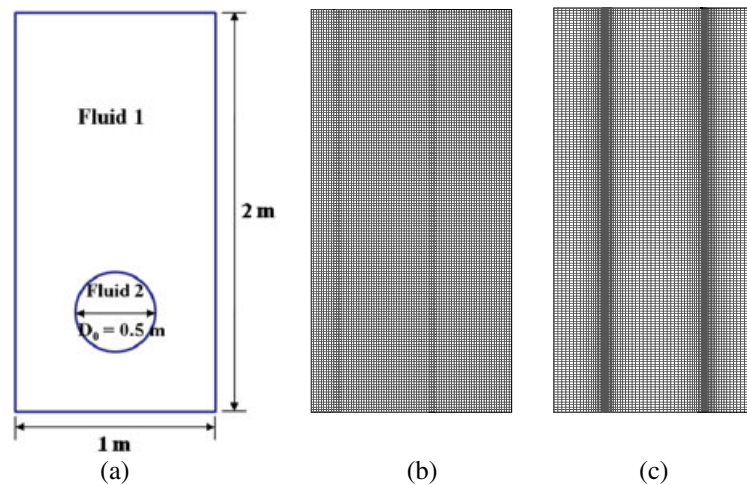


Figure 12. (a) Initial configuration, (b)  $161 \times 321$  uniform grid, (c)  $161 \times 321$  nonuniform grid for 2D bubble rising test cases.

Table V. Mass errors for Case A in which a bubble is rising in a fully filled container.

	Grid size					
	$41 \times 81$		$81 \times 161$		$161 \times 321$	
	Uniform	Nonuniform	Uniform	Nonuniform	Uniform	Nonuniform
Mass error (%)	13.13	11.45	6.20	5.14	2.32	1.78

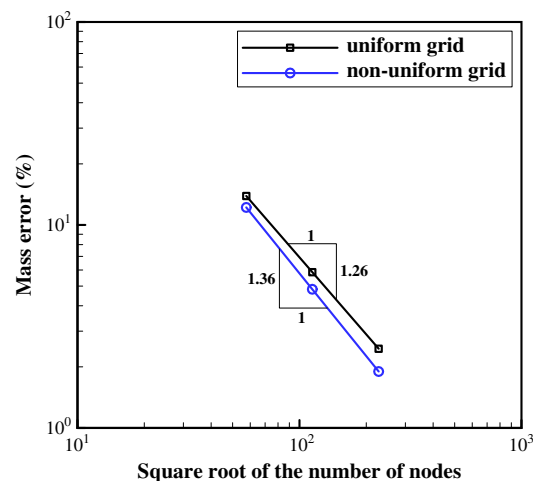


Figure 13. Mass errors for Case A.

### 3.4. Bubble rising in a fully filled container with water

Most of the studies on the 2D bubble rising problem were conducted only to compare the interface shape with reference solutions from other numerical methods or experimental results such as the bubble diagrams produced by Clift *et al.* [36] and Bhaga and Weber [37] without quantitative assessment. Recently, Hysing *et al.* [11] emphasized the necessity for quantitative comparison. Thus, in the present study, two topological parameters such as center of mass and circularity, and a kinematical parameter such as rising velocity were investigated, comparing with those of Hysing *et al.* [11] for two cases. Fluid properties,  $Re$ , and  $Bo$  for the two test cases are shown in Table IV. These benchmark problems were chosen to track the evolution of a rising 2D bubble. We initially

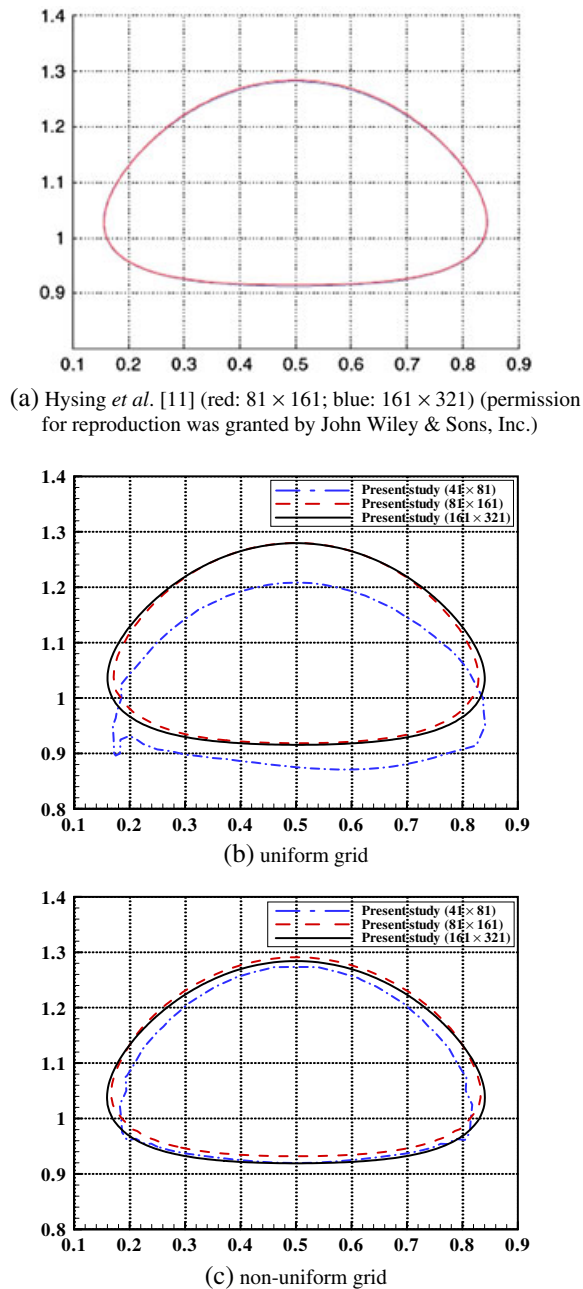
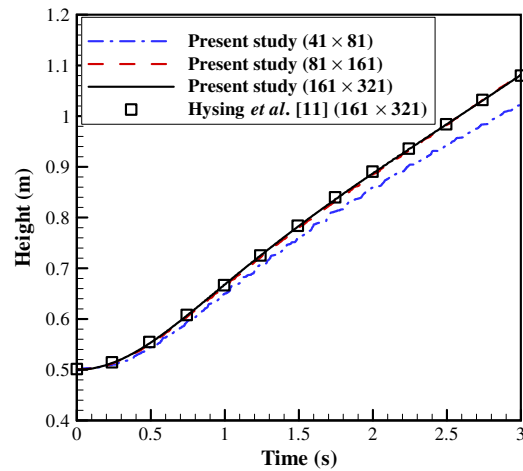


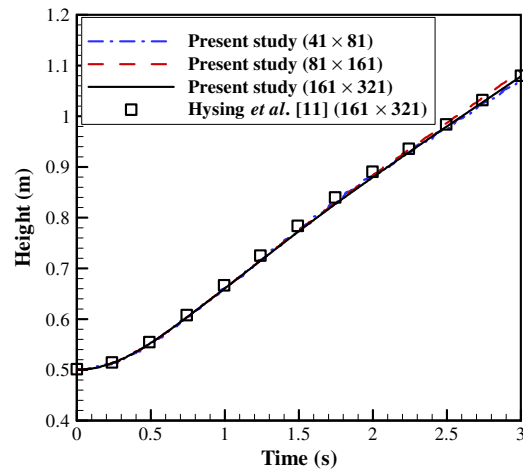
Figure 14. Bubble shapes for Case A.

placed a circular bubble of diameter  $D_0 = 0.5$  m centered at (0.5 m, 0.5 m) in a  $1 \times 2$  m rectangular domain with uniform and nonuniform grids as shown in Figure 12. Slip condition was imposed on vertical walls and no-slip condition on horizontal walls. Computations were conducted until  $t = 3$  s with a time step of 0.002 s. The following parameters were considered to compare the results quantitatively:

- (1) Center of mass: Generally, centroid or center of mass can be used to track the translation of a bubble.



(a) uniform grid



(b) non-uniform grid

Figure 15. Center of mass for Case A.

Table VI. Vertical position of the centroid at  $t = 3$  s for Case A.

	Grid size					
	41 × 81		81 × 161		161 × 321	
	Uniform	Nonuniform	Uniform	Nonuniform	Uniform	Nonuniform
Vertical position of the Centroid (m)	1.02	1.07	1.08	1.09	1.08	1.08



$$y_c = \frac{\int y d\Omega_{\text{fluid } 2}}{\int 1 d\Omega_{\text{fluid } 2}}, \quad (14)$$

where  $\Omega_{\text{fluid } 2}$  denotes the region that the bubble occupies.

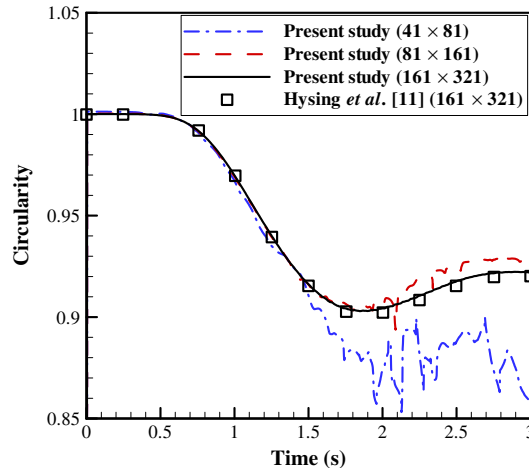
(2) Circularity:

$$C = \frac{P_a}{P_b} = \frac{\text{perimeter of an area-equivalent circle}}{\text{perimeter of a bubble}} = \frac{\pi D_a}{P_b}, \quad (15)$$

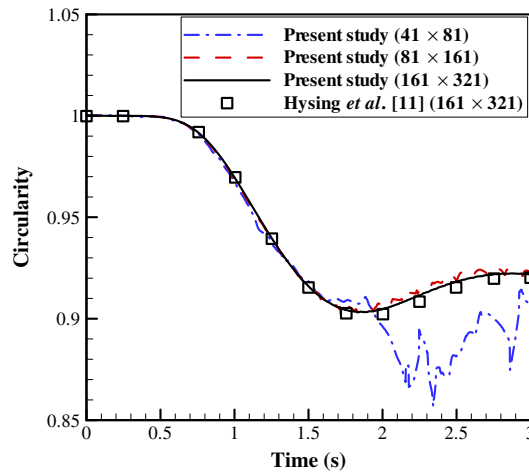
where  $P_a$  denotes the perimeter of a circular bubble with diameter  $D_a$ , which has an area equal to that of a deformed bubble with perimeter  $P_b$ . For the initial circular bubble, the circularity is equal to one and decreases as deformation of the bubble becomes large.

(3) Rising velocity or terminal velocity:

$$V_c = \frac{\int V d\Omega_{\text{fluid } 2}}{\int d\Omega_{\text{fluid } 2}}. \quad (16)$$



(a) uniform grid



(b) non-uniform grid

Figure 16. Circularity for Case A.

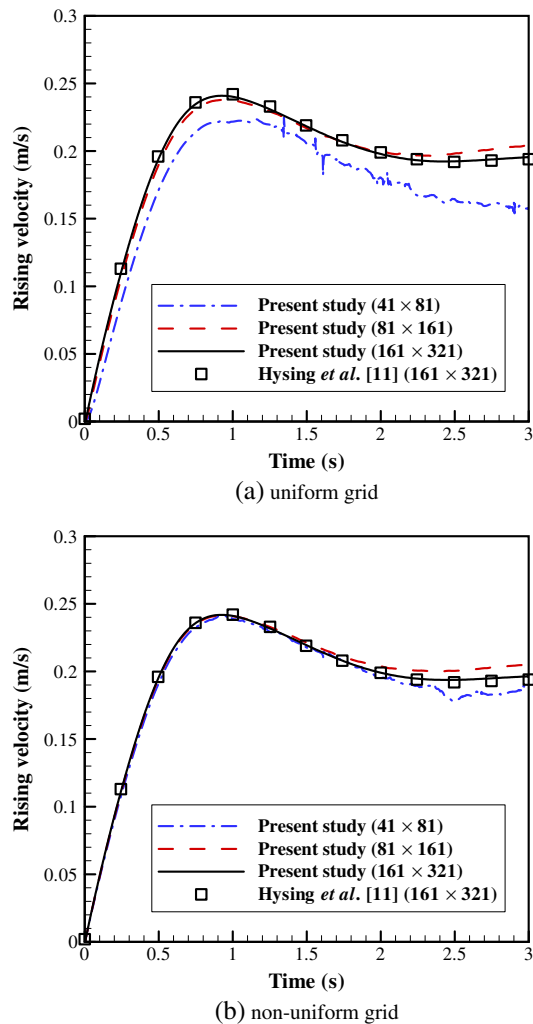


Figure 17. Rising velocity for Case A.

	Grid size					
	41 × 81		81 × 161		161 × 321	
	Uniform	Nonuniform	Uniform	Nonuniform	Uniform	Nonuniform
$\ell_{min}$	0.85	0.87	0.89	0.90	0.90	0.90
$t \ell = \ell_{min}$	2.13 s	2.18 s	2.09 s	1.83 s	1.9 s	1.88 s
$\ell_{min}$						
Hysing <i>et al.</i> [11]		0.91		0.90		0.90
$t \ell = \ell_{min}$						
Hysing <i>et al.</i> [11]		1.84 s		1.91 s		1.88 s
$U$	0.22	0.24	0.24	0.24	0.24	0.24
$t U = U_{max}$	0.93 s	0.95 s	0.94 s	0.93 s	0.93 s	0.92 s
$U$						
Hysing <i>et al.</i> [11]		0.24		0.24		0.24
$t U = U_{max}$						
Hysing <i>et al.</i> [11]		0.90		0.94 s		0.93 s

The mean velocity with which a bubble is rising or moving is a particularly interesting parameter because it measures not only the behavior of the interface tracking algorithm but also the quality of the overall solution.

Table VIII. Mass errors for various time-steps with a uniform  $161 \times 321$  grid.  
( $Re = 35$ ,  $Bo = 10$ ,  $\Delta t_{num}^{ca} = 1.0E-3$  s).

Time-step size (s)	0.006	0.004	0.002	0.001
Mass error (%)	$x$	-0.51	-2.32	-3.42

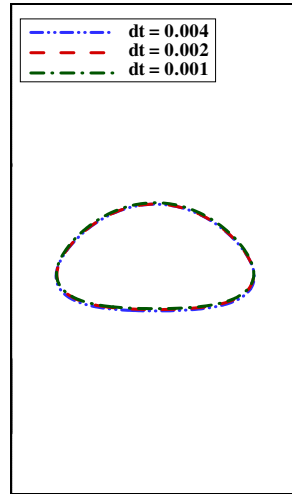


Figure 18. Shapes of the bubble for  $161 \times 321$  uniform grid at  $t = 3$  s for Case A.

Table IX. Mass errors for Case B involving the rising bubble.

	Grid size					
	$41 \times 81$		$81 \times 161$		$161 \times 321$	
	Uniform	Nonuniform	Uniform	Nonuniform	Uniform	Nonuniform
Mass error (%)	11.16	9.37	5.55	3.96	2.09	1.27

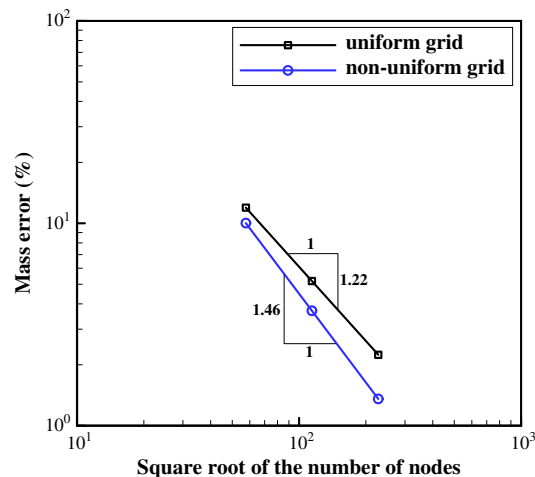
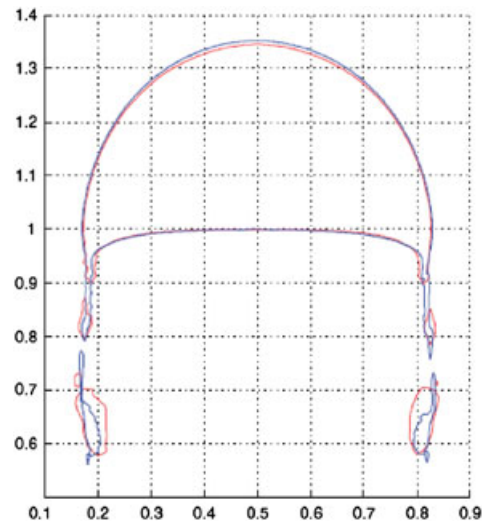
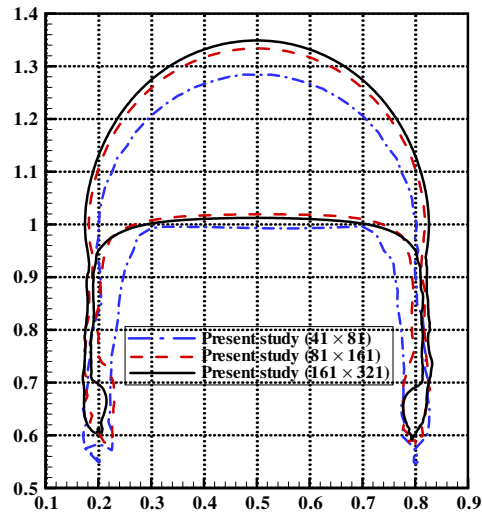


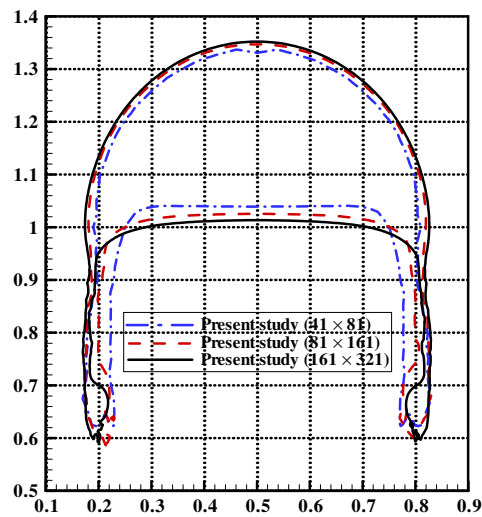
Figure 19. Mass errors for Case B.



(a) Hysing et al. [11] (red:  $81 \times 161$ ; blue:  $161 \times 321$ ) (permission for reproduction was granted by John Wiley & Sons, Inc.)

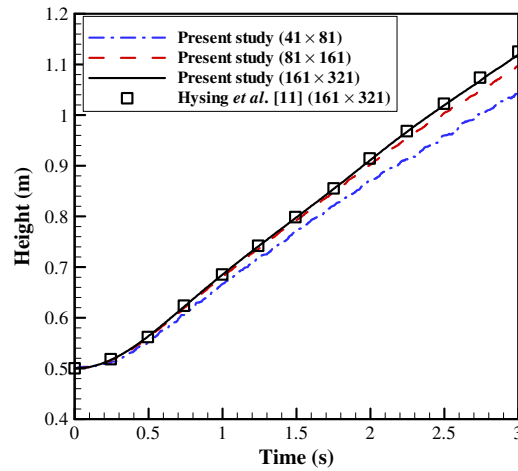


(b) uniform grid

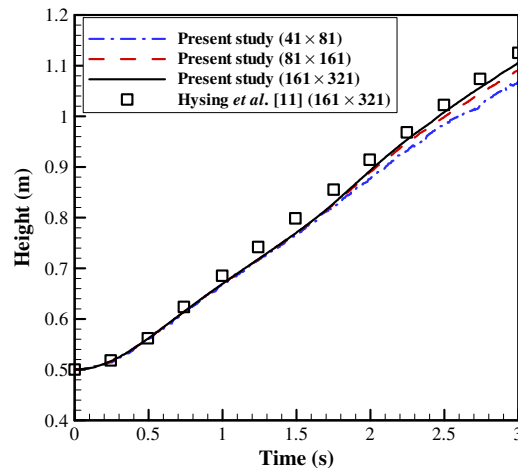


(c) non-uniform grid

**3.4.1. Test Case A.** Computations were conducted at  $Re = 35$  and  $Bo = 10$  with three uniform and nonuniform  $41 \times 81$ ,  $81 \times 161$ , and  $161 \times 321$  grids, respectively. Table V shows mass errors for different grid resolutions. As the grid resolution increased, the mass error decreased, as revealed in Table V and Figure 13 for two grid types. The convergence rates for mass conservation were approximately 1.26 and 1.36 for uniform and nonuniform grids, respectively. The result from the nonuniform grid was slightly better than that from the uniform one in terms of mass conservation. For the nonuniform case, smaller elements were used near the region where the curvature of the interface of a bubble was larger as shown in Figure 12. Figure 14 shows the bubble shapes for three



(a) uniform grid



(b) non-uniform grid

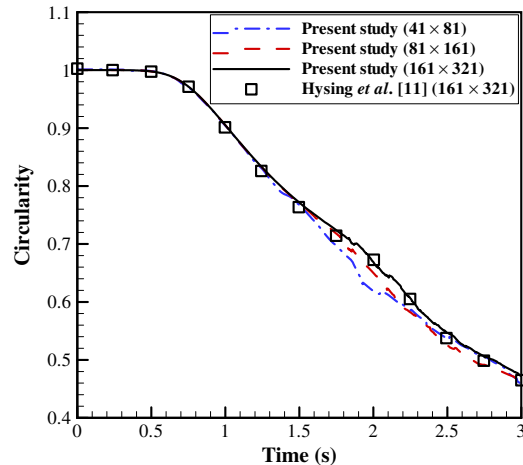
Figure 21. Vertical position of the center of mass for Case B.

Table X. Vertical position of the centroid at  $t = 3$  s for Case B.

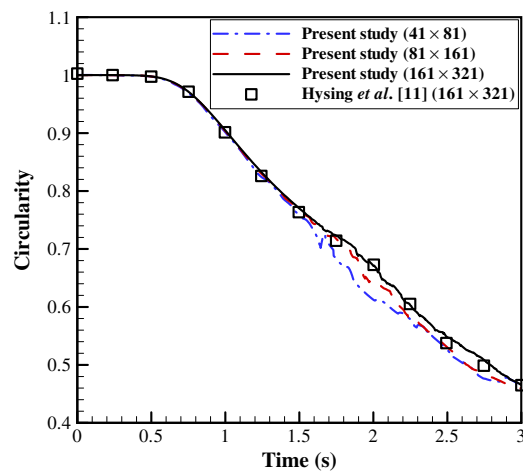
	Grid size					
	$41 \times 81$		$81 \times 161$		$161 \times 321$	
	Uniform	Nonuniform	Uniform	Nonuniform	Uniform	Nonuniform
Vertical position of the centroid (m)	1.041	1.067	1.096	1.091	1.128	1.106

Figure 20. Shapes of the bubble for Case B.

grid resolutions at  $t = 3$  s compared with those of Hysing *et al.* [11]. It was clearly observed that the bubble possessed an ellipsoidal shape when the surface tension was rather large as shown in the experimental studies of Clift *et al.* [36] and that the shape converged as the grid resolution increased. In the case of  $41 \times 81$  coarse grid, the nonuniform grid produced quite an improved result compared to the uniform grid. Next, we used previously defined benchmark quantities for comparison of accuracy. Figure 15 shows the evolution of the center of mass for three grid resolutions. As in Figure 14,



(a) uniform grid



(b) non-uniform grid

Figure 22. Circularity for Case B.

Table XI. Minimum circularity, with corresponding incidence times for Case B. ( $\phi$ : circularity)

	Grid size					
	41 × 81		81 × 161		161 × 321	
	Uniform	Nonuniform	Uniform	Nonuniform	Uniform	Nonuniform
$\phi_{min}$	0.459	0.465	0.463	0.459	0.472	0.466
$t   \phi = \phi_{min}$	3.0 s	3.0 s	3.0 s	3.0 s	3.0 s	3.0 s
$\phi_{min}$						
Hysing <i>et al.</i> [11]		0.487		0.507		0.465
$t   \phi = \phi_{min}$						
Hysing <i>et al.</i> [11]		2.75 s		2.844 s		3.0 s

the solutions of uniform and nonuniform grids agree well with those of Hysing *et al.* [11] when finer grids were used, whereas the nonuniform grid provided a better solution than the uniform one in the case of coarse grid. The vertical position of the centroid at  $t = 3$  s is shown in Table VI for three grid resolutions. The finest grid gave 1.08 m, which was in good agreement with Hysing *et al.* [11]. Figures 16 and 17 show the circularity and rising velocity of the bubble. For the coarsest grid, irregularities existed in the curve because of the low grid resolution. On the other hand, the results of the finest grid ( $161 \times 321$ ) were almost identical to that of Hysing *et al.* [11]. Table VII shows the minimum circularity and maximum rising velocity with the corresponding incidence times for various grids. In terms of the circularity, the maximum deformation of the bubble was created at times  $t = 1.9$  s and 1.88 s, respectively, for the finest uniform and nonuniform grids. Then, the circularity corresponding to the maximum deformation was 0.90 for the two fine grids. The results agreed well with those of Hysing *et al.* [11] as shown in Table VII. Finally, the maximum rising velocity of the two fine grids was 0.24 with incidence times of 0.93 s and 0.92 s for the finest uniform and nonuniform grids, respectively. These results also agree well with those of Hysing *et al.* [11] as shown in Table VII. The time-step restriction calculated by Equation (13) for this case is  $1.0\text{E}-3$  s when a uniform  $161 \times 321$  grid was used. Table VIII shows that the present simulation is stable and mass is conserved well for  $\Delta t \leq 4\Delta t_{\text{num}}^{\text{ca}}$ . Figure 18 also shows that the contours of  $\phi = 0$  obtained using various time-steps with the finest grid are nearly the same at  $t = 3.0$  s.

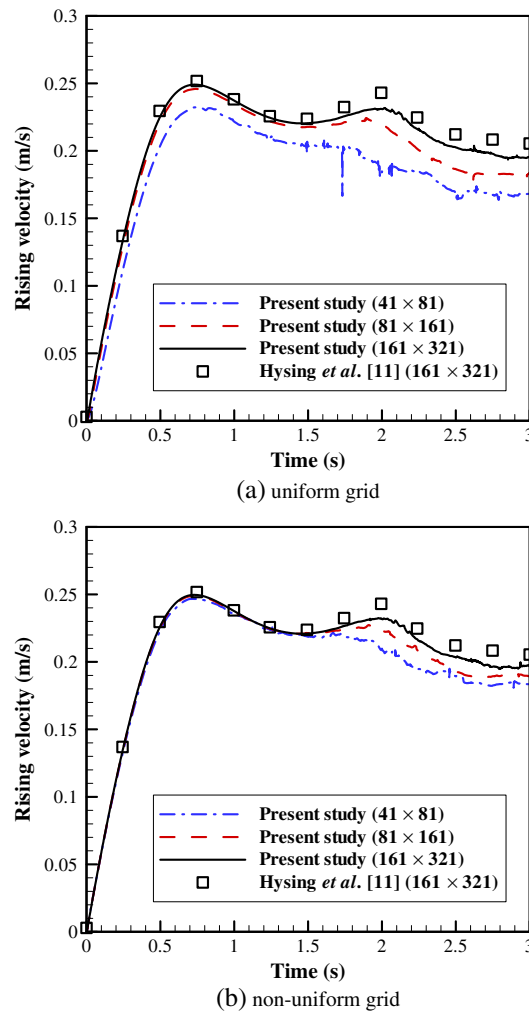


Figure 23. Evolution of rising velocity for Case B.



Table XII. Two peak velocities, with corresponding incidence times for Case B.

	$U_{max1}$ (m/s)	$t U = U_{max1}$ (s)	$U_{max2}$ (m/s)	$t U = U_{max2}$ (s)
Hysing <i>et al.</i> [11]				
(161 × 321 uniform grid)	0.251	0.728	0.244	1.984
Present study				
(41 × 81 uniform grid)	0.232	0.738	0.203	1.738
Present study				
(81 × 161 uniform grid)	0.246	0.742	0.224	1.890
Present study				
(161 × 321 uniform grid)	0.249	0.732	0.232	2.018
Present study				
(41 × 81 nonuniform grid)	0.247	0.714	0.222	1.668
Present study				
(81 × 161 nonuniform grid)	0.249	0.730	0.228	1.952
Present study				
(161 × 321 nonuniform grid)	0.250	0.730	0.233	1.976

**3.4.2. Test Case B.** Next, computations were performed at  $Re = 35$  and  $Bo = 125$  using the same grids as Case A. Table IX indicates maximum mass errors for various grid resolutions during the entire simulation. As the grid resolution increased, the mass error decreased, as shown in Table IX and Figure 19. The convergence rates for mass conservation were approximately 1.22 and 1.46 for uniform and nonuniform grids, respectively. In Figure 20, the bubble shapes produced at time  $t = 3$  s with various grids were compared. Unlike the results of Hysing *et al.* [11], our simulations do not show satellite bubbles. As the grid resolution increased, the filaments in tails of the main bulk became thinner, as shown in Figure 20. Figure 21 shows the evolution of the center of mass. The simulations with nonuniform grid seemed to be slightly better when a coarse grid was used. The maximum height of the centroid obtained with the finest uniform grid at  $t = 3$  s was 1.125 m, which was in good agreement with Hysing *et al.* [11] as shown in Table X, whereas there were some discrepancies for the other grids. Figure 22 shows the evolution of the circularity. The present results obtained with the finest grids agreed well with that of Hysing *et al.* [11]. The minimum circularities of the bubble were 0.472 and 0.466 for the finest uniform and nonuniform grids, respectively, which are almost identical to that of Hysing *et al.* [11] as shown in Table XI. It was also revealed that the present simulation was less sensitive to grid resolution than that of Hysing *et al.* [11]. Finally, Figure 23 shows the evolution of rising velocity, in which two peaks exist for the finest grids. The primary peak of rising velocity obtained with the finest grid was in good agreement with that of Hysing *et al.* [11] as shown in Table XII, whereas the secondary peak was a little lower than that of Hysing *et al.* [11], which is presumably due to the difference in the shape of the bubble tail.

#### 4. CONCLUSION

In the present study, a Q2Q1 finite element/level-set method was proposed for simulating incompressible rising bubbles with surface tension. The incompressible Navier–Stokes equation was solved using the Galerkin method for spatial discretization and the Crank–Nicolson method for temporal discretization. The level-set variable was interpolated quadratically when calculating curvature, and linearly using a ‘pseudo’ Q2Q1 finite element when calculating the density and viscosity of a fluid to avoid an unbounded density and viscosity. The advection and reinitialization of the level-set function were calculated by Taylor–Galerkin method and the direct approach method proposed by Cho *et al.* [21], respectively. The effect of surface tension was treated in an explicit way using the CSF model [9]. The accuracy and stability of the present method were investigated in terms of mass conservation and time step. The solutions of the present method are comparable to the existing results, which show a convergence rate between 1.0 and 1.5 orders spatially in terms of mass error. Furthermore, the present method provided stable solutions for rising bubble problems with large

density difference and surface tension effect even when a larger time step than a critical one is used, which is imposed due to the explicit treatment of surface tension.

#### ACKNOWLEDGEMENTS

This work was supported partially by Priority Research Centers Program through the National Research Foundation (NRF) funded by the Ministry of Education, Science and Technology (MEST) (No. 0420-20100115). The corresponding author was supported by Mid-Career Researcher Program through NRF grant funded by the MEST (No. 2009-0079936), Republic of Korea.

#### REFERENCES

1. Sussman MR, Smereka P, Osher S. A level set approach for computing solutions to incompressible two-phase flow. *Journal of Computational Physics* 1994; **114**:146–159.
2. Chang YC, Hou TY, Merriman B, Osher S. A level set formulation of Eulerian interface capturing methods for incompressible fluid flows. *Journal of Computational Physics* 1996; **124**:449–464.
3. Hirt CW, Nichols B D. Volume of Fluid (VOF) method for the dynamics of free boundaries. *Journal of Computational Physics* 1981; **39**:201–225.
4. Pillapakkam SB, Singh P. A level-set method for computing solutions to viscoelastic two-phase flow. *Journal of Computational Physics* 2001; **174**:552–578.
5. Lin C-L, Lee H, Lee T, Weber L J. A level set characteristic Galerkin finite element method for free surface flows. *International Journal of Numerical Methods in Fluids* 2005; **49**:521–547.
6. Marchandise E, Remacle J-F, Chevaugeon N. A quadrature-free discontinuous Galerkin method for the level set equation. *Journal of Computational Physics* 2006; **212**:338–357.
7. Gremaud PA, Kuster CM, Li Z. A study of numerical methods for the level set approach. *Applied Numerical Mathematics* 2007; **57**:837–846.
8. Strain J. Tree methods for moving interfaces. *Journal of Computational Physics* 1999; **151**:616–648.
9. Brackbill JU, Kothe DB, Zemach C. A continuum method for modeling surface tension. *Journal of Computational Physics* 1992; **100**:335–354.
10. Hysing S. A new implicit surface tension implementation for interfacial flows. *International Journal of Numerical Methods in Fluids* 2006; **51**:659–672.
11. Hysing S, Turek S, Kuzmin D, Parolini N, Burman E, Ganesan S, Tobiska L. Quantitative benchmark computations of two-dimensional bubble dynamics. *International Journal of Numerical Methods in Fluids* 2009; **60**:1259–1288.
12. Raessi M, Bussmann M, Mostaghimi J. A semi-implicit finite volume implementation of the CSF method for treating surface tension in interfacial flows. *International Journal of Numerical Methods in Fluids* 2009; **59**:1093–1110.
13. Sussman M, Smith KM, Hussaini MY, Ohta M, Zhi-Wei R. A sharp interface method for incompressible two-phase flows. *Journal of Computational Physics* 2007; **221**:469–505.
14. Ye T, Shyy W, Tai C-F, Chung JN. Assessment of sharp- and continuous-interface methods for drop in static equilibrium. *Computers and Fluids* 2004; **33**:917–926.
15. Tong AY, Wang Z. A numerical method for capillarity-dominant free surface flows. *Journal of Computational Physics* 2007; **221**:506–523.
16. Wang Z, Tong AY. A sharp surface tension modeling method for two-phase incompressible interfacial flows. *International Journal of Numerical Methods in Fluids* 2010; **64**:709–732.
17. Hua J, Lou J. Numerical simulation of bubble rising in viscous liquid. *Journal of Computational Physics* 2007; **222**:769–795.
18. Marchandise E, Geuzaine P, Chevaugeon N, Remacle J-F. A stabilized finite element method using a discontinuous level set approach for the computation of bubble dynamics. *Journal of Computational Physics* 2007; **225**:949–974.
19. Kang M, Fedkiw RP, Liu X-D. A boundary condition capturing method for multiphase incompressible flow. *Journal of Scientific Computing* 2000; **15**:323–360.
20. Fedkiw RP, Aslam T, Merriman B, Osher S. A non-oscillatory Eulerian approach to interfaces in multimaterial flows (the Ghost Fluid Method). *Journal of Computational Physics* 1999; **152**:457–492.
21. Cho MH, Choi HG, Yoo JY. A direct reinitialization approach of level-set/splitting finite element method for simulating incompressible two-phase flows. *International Journal of Numerical Methods in Fluids* 2010. DOI: 10.1002/fld.2437.
22. Tabarrok B, Su J. Semi-implicit Taylor-Galerkin finite element methods for incompressible viscous flows. *Computer Methods in Applied Mechanics and Engineering* 1994; **117**:391–410.
23. Sung J, Choi HG, Yoo JY. Time-accurate computation of unsteady free surface flows using an ALE-segregated equal-order FEM. *Computer Methods in Applied Mechanics and Engineering* 2000; **190**:1425–1440.
24. Mier-Torrecilla M, Idelsohn SR, Oñate E. Advances in the simulation of multi-fluid flows with the particle finite element method. Application to bubble dynamics. *International Journal of Numerical Methods in Fluids*. DOI: 10.1002/fld.2429.
25. Idelsohn SR, Mier-Torrecilla M, Nigro N, Oñate E. On the analysis of heterogeneous fluids with jumps in the viscosity using a discontinuous pressure field. *Computational Mechanics* 2010; **46**:115–124.

26. Hughes TJR, Franca LP, Balestra M. A new finite element formulation for computational fluid dynamics: V. Circumventing the Babuška-Brezzi condition: A stable Petrov-Galerkin formulation of the Stokes problem accommodating equal-order interpolations. *Computer Methods in Applied Mechanics and Engineering* 1986; **59**:85–99.
27. van der Vorst HA. Bi-CGSTAB: A fast and smoothly converging variant of Bi-CG for the solution of nonsymmetric linear systems. *SIAM Journal on Scientific and Statistical Computing* 1992; **13**:631–644.
28. Nam YS, Choi HG, Yoo JY. AILU preconditioning for the finite element formulation of the incompressible Navier-Stokes equations. *Computer Methods in Applied Mechanics and Engineering* 2002; **191**:4323–4339.
29. Donea J. A Taylor-Galerkin method for convective transport problems. *International Journal for Numerical Methods in Engineering* 1984; **20**:101–119.
30. Baker AJ, Kim JW. A Taylor weak-statement algorithm for hyperbolic conservation laws. *International Journal of Numerical Methods in Fluids* 1987; **7**:489–520.
31. Bell JB, Marcus DL. A second-order projection method for variable-density flows. *Journal of Computational Physics* 1992; **101**:334–348.
32. Puckett EG, Almgren AS, Bell JB, Marcus DL, Rider WJ. A high-order projection method for tracking fluid interfaces in variable density incompressible flows. *Journal of Computational Physics* 1997; **130**:269–282.
33. Popinet S, Zaleski S. A front-tracking algorithm for accurate representation of surface tension. *International Journal of Numerical Methods in Fluids* 1999; **30**:775–793.
34. Lafaurie B, Nardone C, Scardovelli R, Zaleski S, Zanetti G. Modelling merging and fragmentation in multiphase flows with surfer. *Journal of Computational Physics* 1994; **113**:134–147.
35. Zhao Y, Tan HH, Zhang B. A high-resolution characteristics-based implicit dual time-stepping VOF method for free surface flow simulation on unstructured grids. *Journal of Computational Physics* 2002; **183**:233–273.
36. Clift R, Grace JR, Weber ME. *Bubbles, Drops, and Particles*. Academic Press: New York, 1978.
37. Bhaga D, Weber ME. Bubbles in viscous liquids: shapes, wakes and velocities. *Journal of Fluid Mechanics* 1981; **105**:61–85.